https://doi.org/10.5194/egusphere-2026-863
Preprint. Discussion started: 26 February 2026

Permian-Triassic redox shift and its ferruginous aftermath in epicontinental seas

Fen Yang[1,2], Sen Li[3]*, Stephen E. Grasby[4], David Bond[5], Ming Pan[1,2], Yadong Sun[3]

[1] Institute of Karst Geology, CAGS/Key Laboratory of Karst Dynamics, MNR & GZAR/International Research Center on Karst under the Auspices of UNESCO, Guilin, Guangxi 541004, China 541004, China.

[2] Pingguo Guangxi, Karst Ecosystem, National Observation and Research Station, Pingguo, Guangxi 531406, China.

[3] State Key Laboratory of Geomicrobiology and Environmental Changes, China University of Geosciences, Wuhan 430074, China.

[4] Geological Survey of Canada, 3303-33rd Street NW, Calgary, Alberta T2L 2A7, Canada.

[5] School of Environmental and Life Sciences, University of Hull, Hull, HU6 7RX, United Kingdom.

Correspondence to: Sen Li (lisen@cug.edu.cn)

Abstract. Marine anoxia has been implicated as a key environmental driver of the end-Permian mass extinction (EPME) and the subsequent prolonged recovery. However, the spatial and temporal extent of oxygen limitation during the EPME interval remains contentious. Here, we present iron speciation, pyrite framboid and molybdenum-uranium (Mo-U) covariation data from two palaeogeographically distinct settings: the Tethyan Chibi section (South China) and the Panthalassian Ursula Creek section (Western Canada) to evaluate redox dynamics across the Permian-Triassic transition. Our data suggest that bottom waters were predominantly dysoxic during the late Changhsingian at both sites. Later, the prevalence of small pyrite framboids, elevated Mo and U enrichment factors ($\mathrm{Mo_{EF}}$ and $\mathrm{U_{EF}}$), and high $\mathrm{Mo_{EF}/U_{EF}}$ ratios near the EPME horizon implicate seafloor anoxia as a key trigger for marine extinctions in epicontinental seas. In the post-extinction Early Triassic, iron speciation and $\mathrm{Mo_{EF}}$-$\mathrm{U_{EF}}$ covariation data reveal a shift to persistently ferruginous conditions in both locations. A global compilation of iron speciation data indicates that anoxic conditions fluctuated between ferruginous and euxinic in epicontinental seas during the Permian-Triassic crisis, with ferruginous conditions expanding significantly in the earliest Triassic. The expansion of a ferruginous seafloor would have limited phosphorus bioavailability, suppressing primary productivity in the immediate aftermath of the EPME, thereby contributing to the slow recovery.

1 Introduction

The end-Permian mass extinction (EPME), ca. 252 Ma, stands as the Phanerozoic's most profound biodiversity crisis and results in a major turnover from Paleozoic to Mesozoic ecosystems (Sepkoski, 1981; Erwin, 2006). An extreme greenhouse climate prevailed during the Early Triassic (Joachimski et al., 2012; Sun et al., 2012), accompanied by extensive oxygen depletion (Isozaki, 1997; Bond and Wignall, 2010; Lau et al., 2016). The post-extinction recovery of marine ecosystems was protracted and punctuated by a series of aborted recoveries, initially characterized by low-complexity communities dominated by calcimicrobes and sparse, low-diversity metazoans. Opportunistic taxa (e.g., small gastropods and bivalves) proliferated globally (Pruss et al., 2006; Chen and Benton, 2012; Foster and Twitchett, 2014).

Marine anoxia has been widely considered a primary mechanism driving the EPME and the subsequent slow, punctuated biotic recovery (Wignall and Hallam, 1992; Takahashi et al., 2009; Grasby et al., 2013). Several competing hypotheses describe the spatio-temporal patterns of oxygen depletion during the EPME. These include the development of global "superanoxia" (Isozaki, 1997; Wignall and Twichett, 2002), the stratification of oceans into oxic surface waters and euxinic (H_2S-rich) deep waters separated by a stable chemocline (e.g., Kump et al., 2005; Meyer et al., 2008), and the expansion of ferruginous [Fe(II)-rich, non-euxinic] conditions (Clarkson et al., 2016). Multiple geochemical proxies point towards the development of persistent or episodic euxinic conditions in Panthalassa and in epicontinental basins. In deep-water settings of Panthalassa (e.g., the rare records of Japan and New Zealand), small pyrite framboids (mean diameters < 5 μm), significant concentrations of redox-sensitive trace elements such as Mo, and negative pyrite sulfur isotope shifts are all indicative of persistent euxinia and restricted water-column ventilation (Shen et al., 2011; Takahashi et al., 2021). Numerous studies demonstrate that euxinic waters invaded shallow epicontinental basins extensively around the Permian-Triassic (P-T) boundary, including equatorial Tethys (e.g., the South China Block), the Gondwanan margin in mid to high latitudes, and the Pangaea northwestern margin (Wignall and Twitchett, 1996; Neilsen et al., 2010; Grasby and Beauchamp, 2008, Lau et al., 2016; Zhang et al., 2017; Stebbins et al., 2019; Xiang et al., 2020). Biomarker evidence from chlorobactene (indicative of green sulfur bacteria) suggests that euxinic waters expanded into the photic zone (Grice et al., 2005; Cao et al., 2009).

In contrast, iron proxies reveal dynamic redox fluctuations between euxinic and ferruginous conditions, exhibiting regional heterogeneity during the EPME. Along the margins of equatorial Tethys (e.g., South China), iron proxies document a shift from the Changhsingian euxinic to Griesbachian ferruginous conditions, as indicated by decreased the proportion of iron bound in pyrite relative to the highly reactive iron pool (Fe_{py}/Fe_{HR}) in multiple stratigraphic records (Xiang et al., 2016, 2020; Lei et al., 2017; Ge et al., 2022). Conversely, strata from the northwestern Pangaea margin reveal a different redox trend, with ferruginous conditions transitioning to euxinic environments across the P-T boundary (e.g., Neilsen et al., 2010; Mettam et al., 2017; Schobben et al., 2020). Meanwhile, Panthalassa experienced predominantly euxinic conditions across the EPME, with intermittent ferruginous intervals developing during the earliest Triassic (Takahashi et al., 2021).

Evidence increasingly suggests that anoxia may have been largely confined to slope settings, with periodic redox oscillations driving transient anoxic episodes in shallow marine environments (Algeo et al., 2010; Shen et al., 2012, 2016; Zhang et al., 2017). Multiple independent proxies—including bioturbation, depletion of Fe_{HR}, absence of pyrite framboids, rare earth element anomalies, and Mo and Tl isotope signatures—indicate intervals with sustained oxygenation of bottom waters regionally around the EPME (Beatty et al., 2008; Proemse et al., 2013; Garbelli et al., 2016; Newby et al., 2021; Chen et al., 2022; Ge and Bond, 2022; Taniwaki et al., 2022; Yang et al., 2024; Frank et al., 2025). These findings challenge the paradigm of globally pervasive anoxia, suggesting instead that oxygen restriction during the EPME was more spatially heterogeneous than previously suggested. While oxic refugia can be reconciled with U-based modelling that suggests only ~20% of the seafloor was anoxic at that time (Lau et al., 2016), there remains an issue that the residence time of U in seawater would not capture transient anoxic events (Grasby et al., 2021).

To further resolve spatial-temporal changes in marine redox states during the EPME, we investigated two Upper Permian to Lower Triassic successions from contrasting palaeogeographic locations: Chibi (equatorial Tethys) and Ursula Creek (northwestern margin of Pangaea). We then synthesize multi-proxy data to evaluate the redox history through the EPME and earliest Triassic in differing settings.

2 Geological settings

Paleogeographic reconstructions indicate that the South China Block was situated in the equatorial eastern Tethys and remained tectonically isolated during the P-T interval (Scotese, 2014; Fig. 1A). During the lates Permian (Changhsingian), sedimentation across the South China Block was characterized by a pronounced platform-basin differentiation, with shallow-water carbonate deposition dominating the Yangtze Platform and siliceous deep-water sediments accumulating along its margins (Feng et al., 1996; Fig. 1B). The Chibi study section (29°45′5.33″N, 113°57′6.75″E) is exposed in the northern marginal basin of the middle Yangtze Platform. It records a continuous P-T stratigraphic succession, encompassing the Wuchiaping and Talung formations (Upper Permian) and extending upward into the Daye Formation (Lower Triassic) (Yang et al., 2022). The Wuchiaping Formation comprises grey, thick-bedded wackestones and packstones containing abundant benthic calcareous bioclasts and chert nodules. It is overlain by the Talung Formation, which is characterized by thin-bedded cherts interbedded with siliceous mudstones, wackestones, and shales and commonly yields radiolarians and sponge spicules. The overlying Daye Formation consists mainly of thin-bedded wackestones interlayered with marls, and the P-T boundary is located 83 cm above its basal contact (Yang et al., 2022).

The Ursula Creek section (55°59′36.54″N, 123°10′27.18″W) is located on the north shore of Williston Lake, a hydroelectric reservoir in British Columbia in the Canadian Rocky Mountains (Fig. 1C). Palaeogeographically, the Ursula Creek section was located on the Pangaea northwestern margin (approximately 30° N) during the P-T interval (Fig. 1A). Previous studies have documented the stratigraphic characteristics of the Ursula Creek section, a deep marine succession that exposes near-vertically dipping strata spanning the Middle Permian to Middle Triassic (Henderson, 1997; Woods et al., 2023). Upper Permian-Lower Triassic strata are assigned to the Fantasque and Grayling formations. The Fantasque Formation is composed predominantly of thinly bedded cherts intercalated with shale layers, and its faunal assemblages are characterized by abundant radiolarians and sponge spicules. The overlying Grayling Formation comprises thinly bedded shales. The P-T boundary was identified at ~80 cm above the base of the Grayling Formation (Wignall and Newton, 2003).

3 Methods

Size distributions of pyrite framboids were determined from 37 prepared thin sections at Ursula Creek using a scanning electron microscope (SEM) at the State Key Laboratory of Geomicrobiology and Environmental Changes, China University of Geosciences (CUG Wuhan). All polished thin sections were sputter-coated with carbon powder to enhance imaging quality. The SEM was operated in backscattered electron mode at 2500 × magnification. The chemical composition of framboids was qualitatively characterized using energy-dispersive spectroscopy (EDS).

For iron proxies, 97 bulk rock samples from the Chibi and Ursula Creek sections were crushed with a jaw crusher and ground by a mixer mill. Total iron (Fe_T) concentrations were determined using X-ray fluorescence (XRF) at the ALS Minerals laboratory located in Guangzhou, achieving a reproducibility better than 0.1 wt% (1σ). Of these, 54 samples showing Fe_T values above 0.5 wt% were used in subsequent Fe speciation extractions. Iron phases associated with carbonates (Fe_{carb}), (oxyhydr)oxides (Fe_{ox}), and magnetite (Fe_{mag}) were sequentially extracted following Poulton and Canfield (2005). Fe_{carb} was removed using 1M Na-acetate (pH 4.5) at 50 °C for 48 h, Fe_{ox} with Na-dithionite (pH 4.8) at room temperature for 2h, and Femag with a solution of 0.2M ammonium oxalate and 0.17M oxalic acid at room temperature for 6h. Fe concentrations were determined using atomic absorption spectrometry at the State Key Laboratory of Geomicrobiology and Environmental Changes, CUG Wuhan. The Fe_{py} was quantified stoichiometrically determined by the weight of precipitated Ag_2S following chromous chloride distillation, as described by Canfield et al. (1986). Replicate extractions of the WHIT international reference material (Alcott et al., 2020) gave a relative standard deviation below 5% for each step.

For trace elements, 75 powdered samples were treated with a mixture of H_2O, HF, $HClO_4$, and HNO_3 (2:2:1:1) for digestion at the Geological Survey of Canada. Analyses of the resulting solutions were quantified by ICP-MS (PerkinElmer), and replicate measurements showed a relative deviation below 2% (2σ). Enrichment factors (EF) for trace elements were obtained by normalizing the sample X/Al ratios to those of the Post-Archean Average Shale (PAAS; Taylor and McLennan, 1985), with X representing Mo and U.

4 Results

4.1 Pyrite framboid analysis

At Ursula Creek, abundant pyrite framboids were observed in 20 of the 37 samples (54.1%; Fig. 2), totaling 2140 individuals measured for this study (see supplementary material). The remaining 17 samples contained either none, or rare pyrite framboids and euhedral pyrite.

https://doi.org/10.5194/egusphere-2026-863
Preprint. Discussion started: 26 February 2026

Mean framboid diameters generally decrease upward in the Fantasque Formation (Fig. 2). Within the lowermost 3 m of the study section, three samples yield mean framboid diameters of 7.9–9.6 μm, with standard deviation (1 σ) ranging from 2.0 to 3.2 μm (Fig. 3). At section height 3–10 m, pyrite framboids are mostly absent except for one sample containing a small quantity (n = 55) of larger framboids (mean = 10.4 μm), a wide size distribution (3.6–25.3 μm), and a standard deviation of 4.7 μm. Numerous framboids are observed within the upper interval of the Fantasque Formation (10–13 m section height), with mean diameters ranging from 6.8 to 9.6 μm and standard deviations between 2.1 and 3.5 μm. Mean diameters decrease slightly at the top of the Fantasque Formation (13–14.3 m section height), ranging from 5.7 to 6.5 μm, with narrow size distribution (1 σ < 3.0 μm). Within the basal ~2.7 m of the overlying Grayling Formation shales (earliest Griesbachian), framboids are absent. Above this interval, numerous small pyrite framboids exist in the Grayling Formation (17.5–31.6 m section height), with mean diameters between 5.3 and 6.5 μm and 1 σ from 1.2 to 2.8 μm. EDS analysis detected about 25 wt% oxygen content in pyrite framboids from the Ursula Creek section (Figs. 4A and B), suggesting partial oxidation rather than stoichiometric FeS_2.

4.2 Fe_T, Fe_T/Al and Fe proxies

At Ursula Creek, Fe_T contents range from 0.2 to 4.7 wt% (mean = 1.3 wt%), with 46 out of 59 samples exceeding 0.5 wt% (Fig. 2). Samples exhibiting $Fe_T < 0.5$ wt% occur exclusively in the lower Fantasque Formation (Fig. 2). Fe_T concentrations in the upper Fantasque Formation show a slight increase, varying from 0.5 to 1.1 wt% (mean = 0.7 wt%). The Grayling Formation exhibits generally higher Fe_T (0.5–4.7 wt%, mean = 2.2 wt%). In samples with $Fe_T > 0.5$ wt%, the Fe_{HR}/Fe_T is generally above 0.6 (mean = 0.9), with one exception of 0.3. The Fe_{py}/Fe_{HR} are low, varying from 0 to 0.7 (mean = 0.1). The Fantasque Formation shows consistently low Fe_{py}/Fe_{HR} ratios (mean = 0.2) while the Grayling Formation has more variable Fe_{py}/Fe_{HR} ratios (0–0.5, mean = 0.1). Notably, the Ursula Creek section records elevated Fe_{ox} contents, and Fe_{ox}/Fe_{HR} ratios span 0.1–0.9, with 28 of 35 values exceeding 0.5. The $(Fe_{ox}+Fe_{py})/Fe_{HR}$ ratios fall within 0.6–0.9 (mean = 0.8), with only two samples displaying values below 0.6. The total Fe relative to aluminum (Fe_T/Al) ratios vary from 0.1 to 2.7 (mean = 0.5), averaging 0.4 in the Fantasque Formation and 0.5 in the more variable Grayling Formation.

At Chibi, Fe_T concentrations vary from 0.1–5.7 wt% (mean = 1.1 wt%), with 25 samples showing values > 0.5 wt% (Fig. 5). Among these, 19 samples were analyzed for iron speciation. Most samples

https://doi.org/10.5194/egusphere-2026-863
Preprint. Discussion started: 26 February 2026

from the lower to middle Talung Formation (*C. subcarinata* and *C. changxingensis* zones) yield $Fe_T <$ 0.5 wt%. Fe_T concentrations increase markedly in the upper Talung Formation (*C. yini-H. praeparvus* Zone), ranging from 0.9 to 5.7 wt%. The Daye Formation generally contained higher Fe_T concentrations than the Talung Formation, with most samples ranging from 0.5 to 2.6 wt% and two samples showing lower values. For samples with $Fe_T > 0.5$ wt%, Fe_{HR}/Fe_T ratios fall between 0.4 to 1.0 (mean = 0.7). The Fe_{Py}/Fe_{HR} ratios in this section span 0.1–0.9 (mean = 0.4), with most values < 0.6 (14 out of 19 samples). Fe_{ox} contents are low, with Fe_{ox}/Fe_{HR} rations < 0.1 in all samples. The Fe_T/Al ratios fall between 0.4 and 6.7, (mean = 1.0) averaging 2.1 in the Talung Formation and a more stable 0.6 in the lower Daye Formation.

4.3 Molybdenum and uranium concentrations, enrichment factors and ratios (Ursula Creek)

At Ursula Creek, Mo and U concentrations, their enrichment factors (Mo_{EF}, U_{EF}), and corresponding ratios (Mo/U, Mo_{EF}/U_{EF}) display similar variations, generally rising from the Late Permian into the Early Triassic (Fig. 2). In the Fantasque Formation (n = 34), Mo concentrations fall between 0.1 and 4.8 ppm (mean = 0.7 ppm), with corresponding Mo_{EF} values span 0.6 to 25.6 (mean = 4.3); most samples (n = 31) show only modest Mo enrichment ($Mo_{EF} < 10$). For U, concentrations fall in the range of 0.2–2.2 ppm (mean = 1.0 ppm), and U_{EF} values range from 1.6 to 17.7 (mean = 6.1). Mo_{EF}/U_{EF} ratios are generally low (0.2–2.2, mean = 0.6), with 25 samples exhibiting values below 0.1 times that of modern seawater, and the remainder falling in the range of 0.1 to 0.3 times seawater (Fig. 6). In contrast, Mo/U ratios are relatively higher than Mo_{EF}/U_{EF} ratios, spanning 0.2–2.4 (mean = 0.7).

In the Grayling Formation (n = 41), all proxies exhibit significantly higher values. For Mo, concentrations and enrichment factors show significantly greater variation from 0.6 to 146.8 ppm (mean = 20.0 ppm) and 2.2 to 175.2 (mean = 29.1), respectively. Most samples (n = 36) show high Mo enrichment (Mo_{EF}: 11.0 to 57.0). One sample displays an extremely high enrichment ($Mo_{EF} > 100$), and four samples show low to modest enrichment ($Mo_{EF} < 10$). In contrast to Mo, U concentrations and enrichment factors exhibit modest variability, with concentrations varying narrowly from 1.3 to 15.0 ppm (mean = 6.0 ppm) and U_{EF} values ranging from 4.6 to 23.4 (mean = 9.9). Mo_{EF}/U_{EF} ratios fall between 0.4 and 8.9 (mean = 2.9). All but one sample have Mo_{EF}/U_{EF} ratios between 0.1 and 1 times that of modern seawater (Fig. 6). Mo/U ratios span 0.5–9.8 (mean = 3.1).

5 Discussion

5.1 Redox evolution

Among various geochemical and sedimentological proxies for distinguishing redox states, pyrite framboid mean size has become established as a reliable method (e.g., Wilkin and Barnes, 1996). The abundance of pyrite framboids typically increases as anoxia develops, accompanied by a decrease in mean diameter and a narrowing of the size distribution. Specifically, the absence of framboids typically indicates local oxic conditions; abundant framboids with mean diameters ranging from 6 to 10 μm suggest dysoxic conditions; abundant framboids with mean diameters below 6 μm reflect anoxic environments, with those below 5 μm pointing to euxinic settings (e.g., Wilkin and Barnes, 1996; Bond and Wignall, 2010).

Iron speciation [e.g., Fe(II), Fe(III), and sulfide-associated phases] exhibits redox-sensitive geochemical behavior, which is widely applied as a proxy to reconstruct palaeo-redox states in ancient depositional settings (e.g., Poulton and Canfield, 2011). To ensure analytical reliability, these proxies are typically applied only to samples with Fe_T concentrations > 0.5 wt% (Clarkson et al., 2014). Modern oxic marine sediments typically exhibit a depletion of Fe_{HR}, as indicated by $Fe_{HR}/Fe_T < 0.22$, which reflects limited authigenic Fe preservation under well-oxygenated conditions (Poulton and Raiswell, 2002). By contrast, under anoxic environments, sediments commonly show substantial enrichment of Fe_{HR} ($Fe_{HR}/Fe_T > 0.38$; Poulton, 2021). Accumulation of H_2S in anoxic bottom waters promotes pyritization of Fe_{HR}, driving $Fe_{py}/Fe_{HR} > 0.8$, an established threshold for euxinic settings. Conversely, $Fe_{py}/Fe_{HR} < 0.6$ is indicative of ferruginous settings, where H_2S availability is limited. When Fe_{py}/Fe_{HR} falls between 0.6 and 0.8, the redox classification becomes ambiguous and further evidence is required (e.g., from independent proxies) to make an informed interpretation (Poulton and Canfield, 2011).

Molybdenum-uranium covariation is widely used to reconstruct palaeo-redox states in ancient depositional environments, owing to the distinct redox-sensitive geochemical behaviors of these elements (e.g., Algeo and Tribovillard, 2009). The application of Mo_{EF} and U_{EF} to non-siliciclastic rocks is subject to potential artifacts, as low detrital Al content can result in elevated values (Tribovillard et al., 2006). Nevertheless, the consistent stratigraphic trends in EFs, elemental concentrations, and their ratios in this study support their reliable application in redox analysis (Fig. 2). Generally, more reducing conditions promote greater enrichment of both elements in sediments, with Mo uptake increasing more

https://doi.org/10.5194/egusphere-2026-863
Preprint. Discussion started: 26 February 2026

rapidly than that of U. Under oxic conditions, both Mo and U show little or no enrichment. In dysoxic environments, Mo and U typically show low and modest enrichment factors (EFs < 10), and U tends to be more enriched than Mo ($U_{EF} > Mo_{EF}$) as a result of U being incorporated near the Fe(II)–Fe(III) redox transition, whereas Mo enrichment generally depends on the availability of free H_2S. Under oxygen-depleted, non-euxinic conditions, both elements exhibit stronger enrichment (EFs > 10), with Mo_{EF}/U_{EF} < 1 × seawater. In contrast, under euxinic conditions characterized by abundant H_2S in the water column, both elements exhibit strong enrichment (EFs > 10); however, Mo is preferentially accumulated, leading to Mo_{EF}/U_{EF} > 1 × seawater.

Redox proxies from the Ursula Creek section indicate prolonged water-column deoxygenation during the Changhsingian at the northwestern margin of Pangaea. Abundant pyrite framboids with relatively large mean diameters (7.9 to 9.6 μm), and low Mo_{EF}/U_{EF} ratios (< 0.1 × seawater) in the basal ~3 meters of the studied Fantasque Formation indicate dysoxic conditions prevailed during deposition (Figs. 2 and 6; Bond and Wignall, 2010; Tribovillard et al., 2012). Though this interval is characterized by low Mo_{EF} (1.0 to 3.8) and low to modest U_{EF} (2.3 to 13.4), the low detrital Al component (0.6 to 2.4 wt%) typical for (bio)chemical sediments (e.g., chert and pure carbonate) results in EF values that appear higher than those in siliciclastic sediments (Tribovillard et al., 2006). From 3 to 8.5 m section height (Fantasque Formation), intense bioturbation, including ichnotaxa belonging to *Diplocraterion*, *Teichichnus*, and *Planolites*, along with low Mo_{EF} (0.7 to 9.0) and U_{EF} (1.9 to 7.1) values, low Al contents (0.6 to 2.5 wt%), low Mo_{EF}/U_{EF} ratios (< 0.1 × seawater), and a general lack of pyrite framboids suggests that oxic to dysoxic bottom waters were established during this part of the Changhsingian (Wignall and Newton, 2003; Fig. 2). Several samples that lack pyrite framboids at a height of 8.5–10 m exhibit $Fe_{HR}/Fe_T > 0.38$, moderately elevated Mo_{EF} (17.4 to 25.6) and U_{EF} (11.7–17.7), with Mo_{EF}/U_{EF} ratios spanning 0.1 to 0.3 times that of seawater, suggestive of anoxic conditions. Considering partial pyrite oxidation detected by EDS (Fig. 4A), it is possible that using Fe_{py}/Fe_{HR} could result in an underestimation of the presence of euxinic conditions, and therefore $(Fe_{ox} + Fe_{py})/Fe_{HR}$ is used to detect potential H_2S accumulation on the seafloor. Consistently low $(Fe_{ox} + Fe_{py})/Fe_{HR}$ values and elevated Fe_{HR}/Fe_T in this interval are indicative of ferruginous conditions (Poulton, 2021; Fig. 2). In the upper Fantasque Formation (10.0 to 14.3 m section height), pyrite framboids reappear and decrease in size up-section. Between 10 and 13 m, relatively large mean framboid diameters (6.8 to 9.6 μm) and modest trace metal enrichment suggest a return to predominantly dysoxic conditions. In the uppermost Fantasque Formation

https://doi.org/10.5194/egusphere-2026-863
Preprint. Discussion started: 26 February 2026

(13.0 to 14.3 m), populations of smaller framboids (mean diameters 5.7 to 6.5 μm) and iron speciation results [$Fe_{HR}/Fe_T < 0.38$; $(Fe_{ox} + Fe_{py})/Fe_{HR} < 0.8$] point to fluctuating dysoxic to episodically anoxic, ferruginous conditions immediately preceding the P-T transition.

In the lower Grayling Formation of Ursula Creek, the majority of samples lack pyrite framboids, defining a short-lived Early Triassic "framboid gap", a phenomenon observed elsewhere and linked to ferruginous conditions or reoxygenation (e.g., Yang et al., 2024). At Ursula Creek, evaluated Fe_{HR}/Fe_T values (> 0.38) during this gap suggest the presence of anoxic conditions. While Fe_{py} concentrations are near zero, $(Fe_{ox} + Fe_{py})/Fe_{HR}$ values are generally beyond 0.8. These iron data, combined with trace metal enrichments and Mo_{EF}/U_{EF} values ranging from 0.1 to 1.0 × seawater, indicate that ferruginous conditions (oxygen-depleted and sulfide-free) prevailed in the earliest Triassic at Ursula Creek, punctuated by brief episodes of dysoxia (Fig. 2).

Previous work on the Chibi section has shown that the Upper Permian Talung Formation accumulated in predominantly dysoxic settings with intermittent anoxic/euxinic episodes, as indicated by abundant siliceous sponge spicules and radiolarians, rare calcareous benthic fossils, and pyrite framboid distributions (Yang et al., 2022; Fig. 5). Unlike at Ursula Creek, framboids at Chibi are well-preserved (Fig. 4C), negating concerns of significant oxidation after deposition and confirming the fidelity of the primary redox signals. Our new iron speciation data confirm this dynamic environment, with the latest Permian characterized by fluctuating euxinic (elevated Fe_{HR}/Fe_T and Fe_{py}/Fe_T values) and ferruginous (elevated Fe_{HR}/Fe_T but comparatively low Fe_{py}/Fe_T values) conditions (Fig. 5). Although the Lower Daye Formation (0 to 2.7 m section height) lacks pyrite framboids, other redox indicators including the presence of laminated, fossil-poor facies, carbonate Ce positive anomalies, evaluated Fe_{HR}, and pyrite depletion collectively suggest the development of Fe(II)-rich, oxygen-depleted environments during the framboid gap interval (Yang et al., 2022; Müller et al., 2023; Fig. 5). The reoccurrence of populations of small framboids (mean diameters 5.6 to 7.2 μm) together with our iron speciation constraints, suggests that ferruginous settings persisted into the earliest Triassic, punctuated by intermittent dysoxic episodes (Yang et al., 2022; Fig. 5).

5.2 P-T oceanic redox variation: causes and consequences

To investigate global redox evolution across the P-T transition, we compiled iron speciation records from slope to basinal sections across Panthalassa, Tethys and the northwestern margin of Pangaea (Fig. 7). The

P-T transition in each section is defined by the initial occurrence of the conodont species *Hindeodus parvus* or, alternatively, the minimum value of the well-known first major P-T negative carbon isotopic excursion (e.g., Yuan et al., 2014; Yang et al., 2022).

The Waiheke section of New Zealand provides one of the few available records from Panthalassa. The elevated Fe_{HR} but low Fe_{py} and Mo/Al collectively suggest ferruginous conditions during the Changhsingian in this area (Grasby et al., 2021; Takahashi et al., 2021; Fig. 7). In bedded cherts of the P-T transition, high Fe_{HR}/Fe_T and U/Al ratios, coupled with strong pyritization and elevated Mo/Al values, indicate the presence of euxinic settings (Takahashi et al., 2021; Fig. 7). Two distinct intervals characterized by evaluated Fe_{HR}/Fe_T, low Fe_{py}/Fe_{HR} and Mo/Al values are suggestive of recurring ferruginous episodes during the P-T transition. In contrast, low Fe_{HR}/Fe_T values (< 0.22) during the earliest Triassic suggest episodes of reoxygenation (Takahashi et al., 2021; Fig. 7).

Stratigraphic records from the northern marginal slopes and basins of South China consistently document a transition from dysoxic/euxinic to ferruginous settings from the Late Permian to Early Triassic (Cao et al., 2009; Xiang et al., 2020; Yang et al., 2024). The Meishan GSSP section offers a particularly well-resolved example. There, evidence of green sulfur bacteria based on biomarkers suggests that euxinic conditions were widespread during the latest Permian (Cao et al., 2009). Several samples from the late Changhsingian part exhibit evaluated Fe_{HR}/Fe_T (> 0.38) and reduced Fe_{py}/Fe_{HR} values (< 0.6), indicating episodic ferruginous conditions (Xiang et al., 2020). In the earliest Triassic, a marked decline in Fe_{py}/Fe_{HR} values further supports stable ferruginous conditions at Meishan (Xiang et al., 2020; Fig. 7). This redox pattern is corroborated by iron speciation data from multiple well-documented sections including Ganxi, Xibeixiang, Chibi, Xiakou, Shangsi and Ruichang, which collectively support the development of regionally extensive ferruginous states in the earliest Triassic with episodic intervals of reoxygenation (Shen et al., 2016; Lei et al., 2017; Xiang et al., 2016; Ge et al., 2022; Yang et al., 2024; Fig. 7).

Iron speciation constraints from the Arabian Margin (Oman and the United Arab Emirates) in western Neo-Tethys, and from the Xiang-Qian-Gui Basin of South China, similarly point to iron-rich, oxygen-depleted marine environments prevailing from the end of the Permian into the earliest Triassic, interrupted by short-lived oxygenation pulses during the Changhsingian (Clarkson et al., 2016; Xiang et al., 2022; Yang et al., 2024).

The redox evolution along the northwestern margin of Pangaea exhibits significant spatial heterogeneity. The Ursula Creek section records a transition from dysoxic conditions in the Changhsingian to ferruginous conditions in the Griesbachian. In contrast, sections in Spitsbergen (Festningen, Deltadalen) and Greenland (Fiskegrav) document an opposing trend: a shift from ferruginous conditions to euxinia (Bond and Wignall, 2010; Mettam et al., 2017; Schobben et al., 2020; Fig. 7).

These compiled records reveal a spatially heterogeneous and temporally dynamic global redox landscape across the P-T transition. During the latest Permian, ferruginous conditions intermittently developed across different ocean basins. In the earliest Triassic, however, ferruginous conditions expanded significantly, particularly within Tethys. This expansion may have been driven by a combination of processes: 1) extensive deposition of Late Permian evaporites and intensified anoxia accompanied by enhanced pyrite burial drew down the oceanic sulphate reservoir (Luo et al., 2010; Warren, 2010); 2) strong ocean stratification and sluggish circulation suppressed nutrient upwelling and marine primary productivity, thereby reducing organic-carbon fluxes and limiting microbial sulphate reduction (e.g., Song et al., 2014; Clarkson et al., 2016; Sun, 2024); and 3) intense weathering of Fe-bearing silicate minerals under the Early Triassic extreme greenhouse delivered abundant Fe_{HR} to the oceans, resulting in a marked rise in Fe_{HR} input over sulphate (e.g., Poulton and Canfield, 2011).

The widespread development of ferruginous conditions in early Triassic may have significantly impacted nutrient dynamics, with phosphorus (P) cycling being a key mediator—consistent with observations from past oceanic anoxic events (Papadomanolaki et al., 2022). Enhanced chemical weathering on land in the aftermath of the P-T transition likely boosted detrital delivery to the oceans (Sheldon, 2006; Algeo and Twitchett, 2010; Sun et al., 2018). However, despite the enhanced detrital delivery, marine primary productivity appears not to have risen over this period (e.g., Grasby et al., 2016, 2020; Müller et al., 2022; Sun, 2024). This somewhat contradictory scenario could be attributed to strong thermal ocean stratification that inhibited upwelling and vertical mixing (Grasby et al., 2016; Knies et al., 2022). Additionally, the observed covariation between redox conditions and primary productivity across the P-T transition—where productivity was lower under ferruginous conditions and higher under euxinic conditions—suggests that the widespread ferruginous conditions in the Early Triassic likely imposed an additional constraint on primary production (e.g., Müller et al., 2022; Schobben et al., 2020; Ge et al., 2022; Woods et al., 2023). This productivity contrast may reflect differences in the bioavailability of P, whose biogeochemical behavior is strongly controlled by redox state. Euxinic

https://doi.org/10.5194/egusphere-2026-863
Preprint. Discussion started: 26 February 2026

conditions enhance the P recycling through preferential organic matter preservation and suppressed authigenic apatite formation; this elevates bioavailable P fluxes, and stimulates productivity, which in turn maintains prolonged ocean deoxygenation (Ingall et al., 1993; Papadomanolaki et al., 2022). In contrast, ferruginous environments could have inhibited the recycling of bioavailable P through precipitation of Fe(II)-bearing phosphates (e.g., vivianite), incorporation into green-rust phases, and co-precipitation with iron oxides (Bjerrum and Canfield, 2002; Zegeye et al., 2012; Xiong et al., 2019), although direct mineralogical evidence for ferrous phosphates has not yet been identified from the P-T interval. Therefore, oxygen depletion, together with the potential linkage between ferruginous conditions and nutrient limitation, may have been instrumental in triggering the EPME and delaying the recovery.

6 Conclusions

Permian-Triassic records from equatorial eastern Tethys (Chibi, South China) and the northwestern margin of Pangaea (Ursula Creek, western Canada) record redox evolution across this major transition in Earth history. A multi-proxy approach combining pyrite framboid size distributions, iron speciation results, and Mo-U covariation suggests that predominantly dysoxic bottom waters that were established during the latest Permian in each of these palaeogeographically distinct locations gave way to intense anoxia near the EPME horizon. In the earliest Triassic, the absence of pyrite framboids, coupled with iron proxies and other redox proxies (Ce-anomalies and Mo-U covariation), points to an expansion of ferruginous conditions in epicontinental settings. The shift from dysoxic to ferruginous conditions implies that the EPME was triggered by oxygen and nutrient limitation under ferruginous anoxia.

Author contributions

All authors have been involved in the present work, have approved the manuscript, and agree to its submission. Fen Yang designed this study. Fen Yang, Yadong Sun, Stephen E. Grasby and David P.G. Bond collected the samples used in this study. Fen Yang completed the data preparation and analysis with the help of Sen Li. The manuscript was mainly written by Fen Yang and Sen Li with contributions from all authors. Sen Li is designated as the main corresponding author: lisen@cug.edu.cn.

Competing interests

The authors confirm that there are no financial or personal affiliations that could be perceived as influencing the results presented in this study.

Financial support

This work was jointly supported by the National Natural Science Foundation of China (Grant No. 42272022), the China Postdoctoral Science Foundation (grants No. 2025M770406), the geological survey projects of the China Geological Survey (Grants DD202501029, DD20242650). DPGB acknowledges NERC Grant NE/V001639/1.

References

Alcott, L. J., Krause, A. J., Hammarlund, E. U., Bjerrum, C. J., Scholz, F., Xiong, Y., Hobson, A. J., Neve, L., Mills, B. J. W., März, C., Schnetger, B., Bekker, A., and Poulton, S. W.: Development of Iron Speciation Reference Materials for Palaeoredox Analysis, Geostand. Geoanal. Res., 44, 581–591, https://doi.org/10.1111/ggr.12342, 2020.

Algeo, T. J. and Ingall, E.: Sedimentary Corg:P ratios, paleocean ventilation, and Phanerozoic atmospheric pO_2, Palaeogeogr. Palaeoclimatol. Palaeoecol., 256, 130–155, https://doi.org/10.1016/j.palaeo.2007.02.029, 2007.

Algeo, T. J. and Li, C.: Redox classification and calibration of redox thresholds in sedimentary systems, Geochim. Cosmochim. Acta., 287, 8–26, https://doi.org/10.1016/j.gca.2020.01.055, 2020.

Algeo, T. J. and Tribovillard, N.: Environmental analysis of paleoceanographic systems based on molybdenum–uranium covariation, Chem. Geol., 268, 211–225, https://doi.org/10.1016/j.chemgeo.2009.09.001, 2009.

Algeo, T. J. and Twitchett, R. J.: Anomalous Early Triassic sediment fluxes due to elevated weathering rates and their biological consequences, Geology, 38, 1023–1026, https://doi.org/10.1130/G31203.1, 2010.

Algeo, T. J., Hinnov, L., Moser, J., Maynard, J. B., Elswick, E., Kuwahara, K., and Sano, H.: Changes in productivity and redox conditions in the Panthalassic Ocean during the latest Permian, Geology, 38, 187–190, https://doi.org/10.1130/G30483.1, 2010.

Beatty, T. W., Zonneveld, J. P., and Henderson, C. M.: Anomalously diverse Early Triassic ichnofossil assemblages in northwest Pangea: A case for a shallow-marine habitable zone, Geology, 36, 771–774, https://doi.org/10.1130/G24952A.1, 2008.

Bjerrum, C. J. and Canfield, D. E.: Ocean productivity before about 1.9 Gyr ago limited by phosphorus adsorption onto iron oxides, Nature, 417, 159–162, https://doi.org/10.1038/417159a, 2002.

Bond, D. P. G. and Wignall, P. B.: Pyrite framboid study of marine Permian–Triassic boundary sections: A complex anoxic event and its relationship to contemporaneous mass extinction, GSA Bulletin., 122, 1265–1279, https://doi.org/10.1130/B30042.1, 2010.

Canfield, D. E., Raiswell, R., Westrich, J. T., Reaves, C. M., and Berner, R. A.: The use of chromium reduction in the analysis of reduced inorganic sulfur in sediments and shales, Chem. Geol., 54, 149–155, https://doi.org/10.1016/0009-2541(86)90078-1, 1986.

Canfield, D. E., Poulton, S. W., Knoll, A. H., Narbonne, G. M., Ross, G., Goldberg, T., and Strauss, H.: Ferruginous Conditions Dominated Later Neoproterozoic Deep-Water Chemistry, Science, 321, 949–952, https://doi.org/10.1126/science.1154499, 2008.

Cao, C., Love, G. D., Hays, L. E., Wang, W., Shen, S., and Summons, R. E.: Biogeochemical evidence for euxinic oceans and ecological disturbance presaging the end-Permian mass extinction event, Earth Planet. Sci. Lett., 281, 188–201, https://doi.org/10.1016/j.epsl.2009.02.012, 2009.

Chen, Z. Q. and Benton, M. J.: The timing and pattern of biotic recovery following the end-Permian mass extinction, Nature Geosci., 5, 375–383, https://doi.org/10.1038/ngeo1475, 2012.

Chen, Z. Q., Fang, Y., Wignall, P. B., Guo, Z., Wu, S., Liu, Z., Wang, R., Huang, Y., and Feng, X.: Microbial Blooms Triggered Pyrite Framboid Enrichment and Oxygen Depletion in Carbonate Platforms Immediately After the Latest Permian Extinction, Geophys. Res. Lett., 49, e2021GL096998, https://doi.org/10.1029/2021GL096998, 2022.

Clarkson, M. O., Poulton, S. W., Guilbaud, R., and Wood, R. A.: Assessing the utility of Fe/Al and Fe-speciation to record water column redox conditions in carbonate-rich sediments, Chem. Geol., 382, 111–122, https://doi.org/10.1016/j.chemgeo.2014.05.031, 2014.

Clarkson, M. O., Wood, R. A., Poulton, S. W., Richoz, S., Newton, R. J., Kasemann, S. A., Bowyer, F., and Krystyn, L.: Dynamic anoxic ferruginous conditions during the end-Permian mass extinction and recovery, Nat Commun., 7, 12236, https://doi.org/10.1038/ncomms12236, 2016.

Derry, L. A.: Causes and consequences of mid-Proterozoic anoxia, Geophys. Res. Lett., 42, 8538–8546, https://doi.org/10.1002/2015GL065333, 2015.

https://doi.org/10.5194/egusphere-2026-863
Preprint. Discussion started: 26 February 2026

Erwin, D. H.: Extinction: How life on Earth nearly ended 250 million years ago, Princeton University Press, Princeton, NJ, US, viii, 296 pp., 2006.

Feng, Z. Z., Yang, Y. Q., Jin, Z. K., He, Y. B., Wu, S. H., Xin, W. J., Bao, Z. D., and Tan, J.: Lithofacies paleogeography of the Permian of South China. Acta Sedimentol. Sin.14 (2), 1–11, 1996 (in Chinese with English abstract).

Foster, W. J. and Twitchett, R. J.: Functional diversity of marine ecosystems after the Late Permian mass extinction event, Nature Geosci., 7, 233–238, https://doi.org/10.1038/ngeo2079, 2014.

Frank, A. B., Karapunar, B., Grasby, S. E., Koşun, E., Lahajnar, N., Gómez Correa, M. A., Buchwald, S. Z., Metzke, M., and Foster, W. J.: Assessing the role of anoxia as a potential extinction driver in the shallow marine Neotethys during the Permian-Triassic mass extinction, Chem. Geol., 696, 123108, https://doi.org/10.1016/j.chemgeo.2025.123108, 2025.

Garbelli, C., Angiolini, L., Brand, U., Shen, S., Jadoul, F., Posenato, R., Azmy, K., and Cao, C.: Neotethys seawater chemistry and temperature at the dawn of the end Permian mass extinction, Gondwana Res., 35, 272–285, https://doi.org/10.1016/j.gr.2015.05.012, 2016.

Ge, X., Chen, D., Zhang, G., Huang, T., Liu, M., and El-Shafeiy, M.: Marine redox evolution and organic accumulation in an intrashelf basin, NE Sichuan Basin during the Late Permian, Mar. Pet. Geol., 140, 105633, https://doi.org/10.1016/j.marpetgeo.2022.105633, 2022.

Ge, Y. and Bond, D. P. G.: Two deep marine oxygenation events during the Permian-Triassic boundary interval in South China: Relationship with ocean circulation and marine primary productivity, Earth-sci. Rev., 234, 104220, https://doi.org/10.1016/j.earscirev.2022.104220, 2022.

Georgiev, S. V., Horner, T. J., Stein, H. J., Hannah, J. L., Bingen, B., and Rehkämper, M.: Cadmium-isotopic evidence for increasing primary productivity during the Late Permian anoxic event, Earth Planet. Sci. Lett., 410, 84–96, https://doi.org/10.1016/j.epsl.2014.11.010, 2015.

Grasby, S. E. and Beauchamp, B.: Intrabasin variability of the carbon-isotope record across the Permian–Triassic transition, Sverdrup Basin, Arctic Canada, Chem. Geol., 253, 141–150, https://doi.org/10.1016/j.chemgeo.2008.05.005, 2008.

Grasby, S. E., Beauchamp, B., Embry, A., and Sanei, H.: Recurrent Early Triassic ocean anoxia, Geology, 41, 175–178, https://doi.org/10.1130/G33599.1, 2013.

Grasby, S. E., Beauchamp, B., and Knies, J.: Early Triassic productivity crises delayed recovery from world's worst mass extinction, Geology, 44, 779–782, https://doi.org/10.1130/G38141.1, 2016.

Grasby, S. E., Knies, J., Beauchamp, B., Bond, D. P. G., Wignall, P., and Sun, Y.: Global warming leads to Early Triassic nutrient stress across northern Pangea, GSA Bulletin., 132, 943–954, https://doi.org/10.1130/B32036.1, 2019.

Grasby, S. E., Bond, D. P. G., Wignall, P. B., Yin, R., Strachan, L. J., and Takahashi, S.: Transient Permian-Triassic euxinia in the southern Panthalassa deep ocean, Geology, 49, 889–893, https://doi.org/10.1130/G48928.1, 2021.

Grice, K., Cao, C., Love, G. D., Böttcher, M. E., Twitchett, R. J., Grosjean, E., Summons, R. E., Turgeon, S. C., Dunning, W., and Jin, Y.: Photic Zone Euxinia During the Permian-Triassic Superanoxic Event, Science, 307, 706–709, https://doi.org/10.1126/science.1104323, 2005.

Henderson, C. M.: Uppermost Permian conodonts and the Permian-Triassic boundary in the Western Canada Sedimentary Basin, Bulletin of Canadian Petroleum Geology, 45, 693–707, https://doi.org/10.35767/gscpgbull.45.4.693, 1997.

Hotinski, R. M., Bice, K. L., Kump, L. R., Najjar, R. G., and Arthur, M. A.: Ocean stagnation and end-Permian anoxia, Geology, 29, 7–10, https://doi.org/10.1130/0091-7613(2001)029<0007:OSAEPA>2.0.CO;2, 2001.

Ingall, E. D., Bustin, R. M., and Van Cappellen, P.: Influence of water column anoxia on the burial and preservation of carbon and phosphorus in marine shales, Geochim. Cosmochim. Acta., 57, 303–316, https://doi.org/10.1016/0016-7037(93)90433-W, 1993.

Isozaki, Y.: Permo-Triassic Boundary Superanoxia and Stratified Superocean: Records from Lost Deep Sea, Science, 276, 235–238, https://doi.org/10.1126/science.276.5310.235, 1997.

Joachimski, M. M., Lai, X., Shen, S., Jiang, H., Luo, G., Chen, B., Chen, J., and Sun, Y.: Climate warming in the latest Permian and the Permian–Triassic mass extinction, Geology, 40, 195–198, https://doi.org/10.1130/G32707.1, 2012.

Knies, J., Schönenberger, J., Zwingmann, H., van der Lelij, R., Smelror, M., Vullum, P. E., Brönner, M., Vogt, C., Fredin, O., Müller, A., Grasby, S. E., Beauchamp, B., and Viola, G.: Continental weathering and recovery from ocean nutrient stress during the Early Triassic Biotic Crisis, Commun Earth Environ, 3, 161, https://doi.org/10.1038/s43247-022-00480-z, 2022.

Knoll, A. H., Bambach, R. K., Canfield, D. E., and Grotzinger, J. P.: Comparative Earth History and Late Permian Mass Extinction, Science, 273, 452–457, https://doi.org/10.1126/science.273.5274.452, 1996.

Kump, L. R., Pavlov, A., and Arthur, M. A.: Massive release of hydrogen sulfide to the surface ocean and atmosphere during intervals of oceanic anoxia, Geology, 33, 397–400, https://doi.org/10.1130/G21295.1, 2005.

Lau, K. V., Maher, K., Altiner, D., Kelley, B. M., Kump, L. R., Lehrmann, D. J., Silva-Tamayo, J. C., Weaver, K. L., Yu, M., and Payne, J. L.: Marine anoxia and delayed Earth system recovery after the end-Permian extinction, Proc. Natl. Acad. Sci., 113, 2360–2365, https://doi.org/10.1073/pnas.1515080113, 2016.

Lei, L. D., Shen, J., Li, C., Algeo, T. J., Chen, Z. Q., Feng, Q. L., Cheng, M., Jin, C. S., and Huang, J. H.: Controls on regional marine redox evolution during Permian-Triassic transition in South China, Palaeogeogr. Palaeoclimatol. Palaeoecol., 486, 17–32, https://doi.org/10.1016/j.palaeo.2017.02.010, 2017.

Luo, G., Kump, L. R., Wang, Y., Tong, J., Arthur, M. A., Yang, H., Huang, J., Yin, H., and Xie, S.: Isotopic evidence for an anomalously low oceanic sulfate concentration following end-Permian mass extinction, Earth Planet. Sci. Lett., 300, 101–111, https://doi.org/10.1016/j.epsl.2010.09.041, 2010.

Luo, G., Wang, Y., Grice, K., Kershaw, S., Algeo, T. J., Ruan, X., Yang, H., Jia, C., and Xie, S.: Microbial–algal community changes during the latest Permian ecological crisis: Evidence from lipid biomarkers at Cili, South China, Glob. Planet. Change., 105, 36–51, https://doi.org/10.1016/j.gloplacha.2012.11.015, 2013.

Mettam, C., Zerkle, A. L., Claire, M. W., Izon, G., Junium, C. J., and Twitchett, R. J.: High-frequency fluctuations in redox conditions during the latest Permian mass extinction, Paleogeogr. Paleoclimatol. Paleoecol., 485, 210–223, https://doi.org/10.1016/j.palaeo.2017.06.014, 2017.

Meyer, K. M., Kump, L. R., and Ridgwell, A.: Biogeochemical controls on photic-zone euxinia during the end-Permian mass extinction, Geology, 36, 747–750, https://doi.org/10.1130/G24618A.1, 2008.

Müller, J., Sun, Y., Yang, F., Fantasia, A., and Joachimski, M.: Phosphorus Cycle and Primary Productivity Changes in the Tethys Ocean During the Permian-Triassic Transition: Starving Marine Ecosystems, Front. Earth Sci., 10, https://doi.org/10.3389/feart.2022.832308, 2022.

Müller, J., Sun, Y. D., Yang, F., Regelous, M., and Joachimski, M. M.: Manganous water column in the Tethys Ocean during the Permian-Triassic transition, Glob. Planet. Change., 222, 104067, https://doi.org/10.1016/j.gloplacha.2023.104067, 2023.

Newby, S. M., Owens, J. D., Schoepfer, S. D., and Algeo, T. J.: Transient ocean oxygenation at end-Permian mass extinction onset shown by thallium isotopes, Nat. Geosci., 14, 678–683, https://doi.org/10.1038/s41561-021-00802-4, 2021.

Nielsen, J. K., Shen, Y., Piasecki, S., and Stemmerik, L.: No abrupt change in redox condition caused the end-Permian marine ecosystem collapse in the East Greenland Basin, Earth Planet. Sci. Lett., 291, 32–38, https://doi.org/10.1016/j.epsl.2009.12.043, 2010.

Papadomanolaki, N. M., Lenstra, W. K., Wolthers, M., and Slomp, C. P.: Enhanced phosphorus recycling during past oceanic anoxia amplified by low rates of apatite authigenesis, Sci. Adv., 8, eabn2370, https://doi.org/10.1126/sciadv.abn2370, 2022.

Poulton, S. W.: The low-temperature geochemical cycle of iron: From continental fluxes to marine sediment deposition, Am. J. Sci., 302, 774–805, https://doi.org/10.2475/ajs.302.9.774, 2002.

Poulton, S. W.: The Iron Speciation Paleoredox Proxy, Elements in Geochemical Tracers in Earth System Science, https://doi.org/10.1017/9781108847148, 2021.

Poulton, S. W. and Canfield, D. E.: Development of a sequential extraction procedure for iron: implications for iron partitioning in continentally derived particulates, Chem. Geol., 214, 209–221, https://doi.org/10.1016/j.chemgeo.2004.09.003, 2005.

Poulton, S. W. and Canfield, D. E.: Ferruginous Conditions: A Dominant Feature of the Ocean through Earth's History, Elements, 7, 107–112, https://doi.org/10.2113/gselements.7.2.107, 2011.

Proemse, B. C., Grasby, S. E., Wieser, M. E., Mayer, B., and Beauchamp, B.: Molybdenum isotopic evidence for oxic marine conditions during the latest Permian extinction, Geology, 41, 967–970, https://doi.org/10.1130/G34466.1, 2013.

Pruss, S. B., Bottjer, D. J., Corsetti, F. A., and Baud, A.: A global marine sedimentary response to the end-Permian mass extinction: Examples from southern Turkey and the western United States, Earth-sci. Rev., 78, 193–206, https://doi.org/10.1016/j.earscirev.2006.05.002, 2006.

Schobben, M., Foster, W. J., Sleveland, A. R. N., Zuchuat, V., Svensen, H. H., Planke, S., Bond, D. P. G., Marcelis, F., Newton, R. J., Wignall, P. B., and Poulton, S. W.: A nutrient control on marine anoxia during the end-Permian mass extinction, Nat. Geosci., 13, 640–646, https://doi.org/10.1038/s41561-020-0622-1, 2020.

Schoepfer, S. D., Henderson, C. M., Garrison, G. H., Foriel, J., Ward, P. D., Selby, D., Hower, J. C., Algeo, T. J. and Shen, Y.: Termination of a continent-margin upwelling system at the Permian–Triassic boundary (Opal Creek, Alberta, Canada), Glob. Planet. Change., 105, 21–35, https://doi.org/10.1016/j.gloplacha.2012.07.005, 2013.

https://doi.org/10.5194/egusphere-2026-863
Preprint. Discussion started: 26 February 2026

Scholz, F., McManus, J., and Sommer, S.: The manganese and iron shuttle in a modern euxinic basin and implications for molybdenum cycling at euxinic ocean margins, Chem. Geol., 355, 56–68, https://doi.org/10.1016/j.chemgeo.2013.07.006, 2013.

Scotese, C.: Atlas of Middle & Late Permian and Triassic Paleogeographic Maps, Scotese, C.R., 2014. Atlas of Middle & Late Permian and Triassic Paleogeographic Maps, Maps 43–52, Volumes 3 & 4, PALEOMAP PaleoAtlas for ArcGIS, PALEOMAP Project, Evanston, IL., 2014.

Sepkoski, J. J.: A Factor Analytic Description of the Phanerozoic Marine Fossil Record, Paleobiology, 7, 36–53, 1981.

Sheldon, N. D.: Abrupt chemical weathering increase across the Permian–Triassic boundary, Palaeogeogr. Palaeoclimatol. Palaeoecol., 231, 315–321, https://doi.org/10.1016/j.palaeo.2005.09.001, 2006.

Shen, J., Algeo, T. J., Hu, Q., Zhang, N., Zhou, L., Xia, W., Xie, S., and Feng, Q.: Negative C-isotope excursions at the Permian-Triassic boundary linked to volcanism, Geology, 40, 963–966, https://doi.org/10.1130/G33329.1, 2012.

Shen, J., Feng, Q., Algeo, T. J., Li, C., Planavsky, N. J., Zhou, L., and Zhang, M.: Two pulses of oceanic environmental disturbance during the Permian–Triassic boundary crisis, Earth Planet. Sci. Lett., 443, 139–152, https://doi.org/10.1016/j.epsl.2016.03.030, 2016.

Shen, Y., Farquhar, J., Zhang, H., Masterson, A., Zhang, T., and Wing, B. A.: Multiple S-isotopic evidence for episodic shoaling of anoxic water during Late Permian mass extinction, Nat Commun., 2, 210, https://doi.org/10.1038/ncomms1217, 2011.

Song, H., Tong, J., Algeo, T. J., Song, H., Qiu, H., Zhu, Y., Tian, L., Bates, S., Lyons, T. W., Luo, G., and Kump, L. R.: Early Triassic seawater sulfate drawdown, Geochim. Cosmochim. Acta., 128, 95–113, https://doi.org/10.1016/j.gca.2013.12.009, 2014.

Sperling, E. A., Wolock, C. J., Morgan, A. S., Gill, B. C., Kunzmann, M., Halverson, G. P., Macdonald, F. A., Knoll, A. H., and Johnston, D. T.: Statistical analysis of iron geochemical data suggests limited late Proterozoic oxygenation, Nature, 523, 451–454, https://doi.org/10.1038/nature14589, 2015.

Stebbins, A., Williams, J., Brookfield, M., Nye, S. W., and Hannigan, R.: Frequent euxinia in southern Neo-Tethys Ocean prior to the end-Permian biocrisis: Evidence from the Spiti region, India, Palaeogeogr. Palaeoclimatol. Palaeoecol., 516, 1–10, https://doi.org/10.1016/j.palaeo.2018.11.030, 2019.

Sun, H., Xiao, Y., Gao, Y., Zhang, G., Casey, J. F., and Shen, Y.: Rapid enhancement of chemical weathering recorded by extremely light seawater lithium isotopes at the Permian–Triassic boundary, Proc.

Natl. Acad. Sci., 115, 3782–3787, https://doi.org/10.1073/pnas.1711862115, 2018.

Sun, Y.: Dynamics of nutrient cycles in the Permian–Triassic oceans, Earth-Sci. Rev., 258, 104914, https://doi.org/10.1016/j.earscirev.2024.104914, 2024.

Sun, Y., Joachimski, M. M., Wignall, P. B., Yan, C., Chen, Y., Jiang, H., Wang, L., and Lai, X.: Lethally Hot Temperatures During the Early Triassic Greenhouse, Science, 338, 366–370, https://doi.org/10.1126/science.1224126, 2012.

Takahashi, S., Oba, M., Kaiho, K., Yamakita, S., and Sakata, S.: Panthalassic oceanic anoxia at the end of the Early Triassic: A cause of delay in the recovery of life after the end-Permian mass extinction, Palaeogeogr. Palaeoclimatol. Palaeoecol., 274, 185–195, https://doi.org/10.1016/j.palaeo.2009.01.010, 2009.

Takahashi, S., Hori, R. S., Yamakita, S., Aita, Y., Takemura, A., Ikehara, M., Xiong, Y., Poulton, S. W., Wignall, P. B., Itai, T., Campbell, H. J., and Spörli, B. K.: Progressive development of ocean anoxia in the end-Permian pelagic Panthalassa, Glob. Planet. Change., 207, 103650, https://doi.org/10.1016/j.gloplacha.2021.103650, 2021.

Taniwaki, T., Elders, C., Böttcher, M. E., Holman, A. I., and Grice, K.: Photic zone redox oscillations and microbialite development recorded by Early Triassic sediments of the Perth Basin: A geochemical approach, Geochim. Cosmochim. Acta., 336, 188–207, https://doi.org/10.1016/j.gca.2022.09.011, 2022.

Taylor, S. and McLennan, S.: The Continental Crust: Its Composition and Evolution, Department of Geosciences Faculty Publications, 1985.

Tribovillard, N., Algeo, T. J., Lyons, T., and Riboulleau, A.: Trace metals as paleoredox and paleoproductivity proxies: An update, Chem. Geol., 232, 12–32, https://doi.org/10.1016/j.chemgeo.2006.02.012, 2006.

Tribovillard, N., Algeo, T. J., Baudin, F., and Riboulleau, A.: Analysis of marine environmental conditions based onmolybdenum–uranium covariation—Applications to Mesozoic paleoceanography, Chem. Geol., 324–325, 46–58, https://doi.org/10.1016/j.chemgeo.2011.09.009, 2012.

Warren, J. K.: Evaporites through time: Tectonic, climatic and eustatic controls in marine and nonmarine deposits, Earth Sci. Rev., 98, 217–268, https://doi.org/10.1016/j.earscirev.2009.11.004, 2010.

Wignall, P. and Twitchett, R.: Extent, duration, and nature of the Permian-Triassic superanoxic event, in: Catastrophic events and mass extinctions: impacts and beyond, vol. Special Paper 356, edited by: Koeberl, C. and MacLoed, K., Geological Society of America, 395–413, 2002.

Wignall, P. B. and Hallam, A.: Anoxia as a cause of the Permian/Triassic mass extinction: facies evidence from northern Italy and the western United States, Palaeogeogr. Palaeoclimatol. Palaeoecol., 93, 21–46, https://doi.org/10.1016/0031-0182(92)90182-5, 1992.

Wignall, P. B. and Newton, R.: Contrasting Deep-Water Records from the Upper Permian and Lower Triassic of South Tibet and British Columbia: Evidence for a Diachronous Mass Extinction, Palaios, 18, 153–167, 2003.

Wignall, P. B. and Twitchett, R. J.: Oceanic Anoxia and the End Permian Mass Extinction, Science, 272, 1155–1158, https://doi.org/10.1126/science.272.5265.1155, 1996.

Wilkin, R. T. and Barnes, H. L.: Pyrite formation by reactions of iron monosulfides with dissolved inorganic and organic sulfur species, Geochim. Cosmochim. Acta., 60, 4167–4179, https://doi.org/10.1016/S0016-7037(97)81466-4, 1996.

Wilkin, R. T., Barnes, H. L., and Brantley, S. L.: The size distribution of framboidal pyrite in modern sediments: An indicator of redox conditions, Geochim. Cosmochim. Acta., 60, 3897–3912, https://doi.org/10.1016/0016-7037(96)00209-8, 1996.

Woods, A. D., Zonneveld, J. P., and Wakefield, R.: Hyperthermal-driven anoxia and reduced productivity in the aftermath of the Permian-Triassic mass extinction: a case study from Western Canada, Front. Earth Sci., 11, https://doi.org/10.3389/feart.2023.1323413, 2023.

Xiang, L., Schoepfer, S. D., Zhang, H., Yuan, D., Cao, C., Zheng, Q., Henderson, C. M., and Shen, S.: Oceanic redox evolution across the end-Permian mass extinction at Shangsi, South China, Paleogeogr. Paleoclimatol. Paleoecol. 448, 59–71, https://doi.org/10.1016/j.palaeo.2015.10.046, 2016.

Xiang, L., Zhang, H., Schoepfer, S. D., Cao, C., Zheng, Q., Yuan, D., Cai, Y., and Shen, S.: Oceanic redox evolution around the end-Permian mass extinction at Meishan, South China, Paleogeogr. Paleoclimatol. Paleoecol., 544, 109626, https://doi.org/10.1016/j.palaeo.2020.109626, 2020.

Xiang, L., Schoepfer, S. D., Yuan, D. X., Zheng, Q. F., and Zhang, H.: Oceanic redox evolution across the end-Permian mass extinction at Penglaitan section, South China, Palaeoworld, 31, 93–102, https://doi.org/10.1016/j.palwor.2021.02.003, 2022.

Xiong, Y., Guilbaud, R., Peacock, C. L., Cox, R. P., Canfield, D. E., Krom, M. D., and Poulton, S. W.: Phosphorus cycling in Lake Cadagno, Switzerland: A low sulfate euxinic ocean analogue, Geochim. Cosmochim. Acta., 251, 116–135, https://doi.org/10.1016/j.gca.2019.02.011, 2019.

Yang, F., Sun, Y. D., Frings, P. J., Luo, L., E, J. W., Wang, L. N., Huang, Y. F., Wang, T., Müller, J., and

Xie, S. C.: Collapse of Late Permian chert factories in the equatorial Tethys and the nature of the Early Triassic chert gap, Earth Planet. Sci. Lett., 600, 117861, https://doi.org/10.1016/j.epsl.2022.117861, 2022.

Yang, F., Li, S., An, K.Y., Bond, P.G.D., Ao, R., Wu, X.B., Ma, L.L., and Sun, Y.D.: 2024. Re-Evaluating Water Column Reoxygenation During the End Permian Mass Extinction. Geochem. Geophys. Geosyst. 25, https://doi.org/10.1029/2024gc011779, 2024.

Yuan, D., Shen, S., Henderson, C. M., Chen, J., Zhang, H., and Feng, H.: Revised conodont-based integrated high-resolution timescale for the Changhsingian Stage and end-Permian extinction interval at the Meishan sections, South China, Lithos, 204, 220–245, https://doi.org/10.1016/j.lithos.2014.03.026, 2014.

Zegeye, A., Bonneville, S., Benning, L. G., Sturm, A., Fowle, D. A., Jones, C., Canfield, D. E., Ruby, C., MacLean, L. C., Nomosatryo, S., Crowe, S. A., and Poulton, S. W.: Green rust formation controls nutrient availability in a ferruginous water column, Geology, 40, 599–602, https://doi.org/10.1130/G32959.1, 2012.

Zhang, G., Zhang, X., Hu, D., Li, D., Algeo, T. J., Farquhar, J., Henderson, C. M., Qin, L., Shen, M., Shen, D., Schoepfer, S. D., Chen, K., and Shen, Y.: Redox chemistry changes in the Panthalassic Ocean linked to the end-Permian mass extinction and delayed Early Triassic biotic recovery, Proc. Natl. Acad. Sci. U.S.A., 114, 1806–1810, https://doi.org/10.1073/pnas.1610931114, 2017.

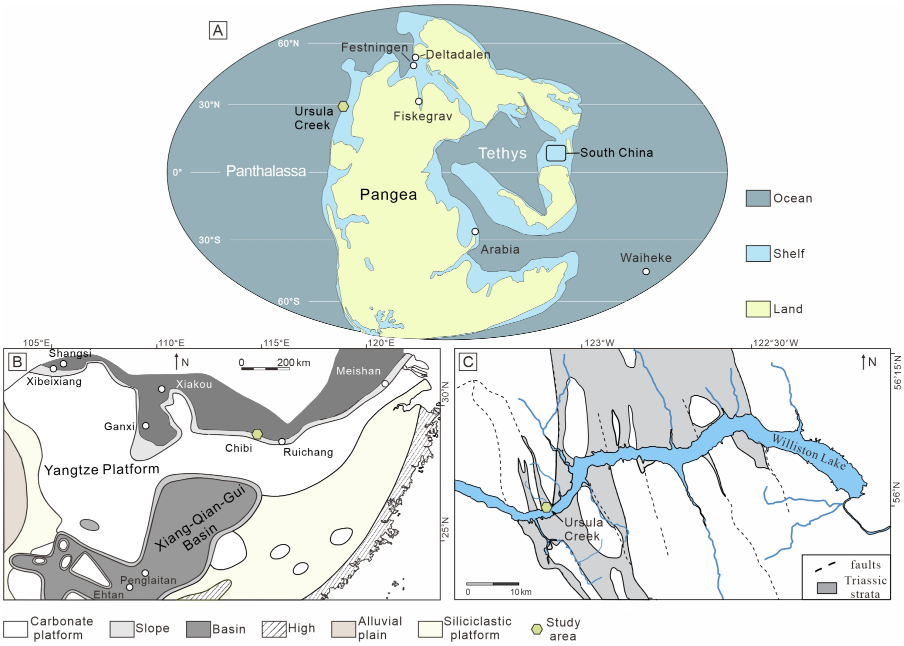

Figure 1. (A) Palaeogeographic reconstruction of Pangaea in the Late Permian (modified from Scotese, 2014). (B) Palaeogeographic reconstruction of the South China Block during the Changhsingian (modified from Feng et al., 1996). (C) Locations of the Ursula Creek section.

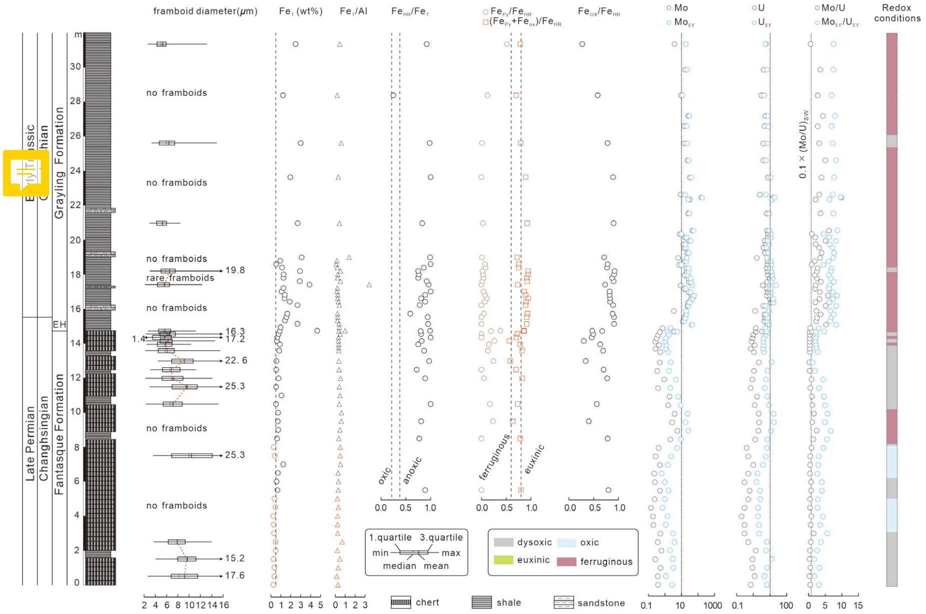

https://doi.org/10.5194/egusphere-2026-863
Preprint. Discussion started: 26 February 2026

Figure 2. Stratigraphic log of the Ursula Creek section with total iron (Fe_T), Fe_T/Al, iron proxies [Fe_{HR}/Fe_T, Fe_{Py}/Fe_{HR}, $(Fe_{Py}+Fe_{ox})/Fe_{HR}$, Fe_{ox}/Fe_{HR}], Mo and U concentrations, enrichment factors (Mo_{EF}, U_{EF}) and their ratios (Mo/U, Mo_{EF}/U_{EF}), and pyrite framboid "box-and-whisker" plots. The "box" represents the interquartile range (25th–75th percentiles) of framboid diameters, the "whiskers" show the minimum and maximum values, and the central lines mark the median and the mean.

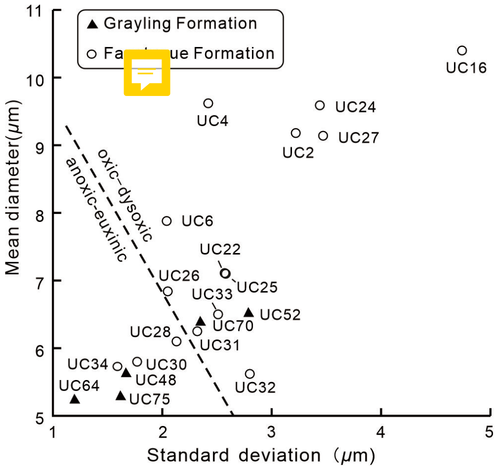

Figure 3. Mean diameter versus standard deviation of framboid size distributions for the Ursula Creek samples. The dashed line separates anoxic-euxinic from oxic-dysoxic conditions (cf. Wilkin et al., 1996).

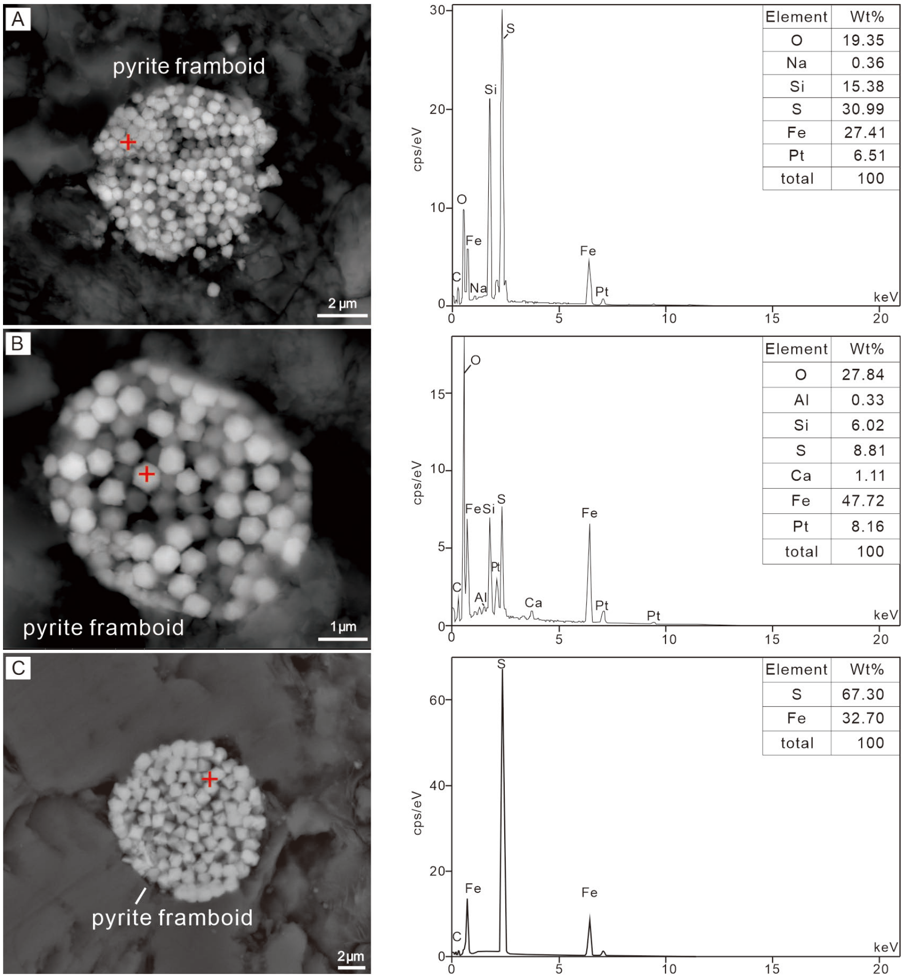

Element	Wt%
O	19.35
Na	0.36
Si	15.38
S	30.99
Fe	27.41
Pt	6.51
total	100

Element	Wt%
O	27.84
Al	0.33
Si	6.02
S	8.81
Ca	1.11
Fe	47.72
Pt	8.16
total	100

Element	Wt%
S	67.30
Fe	32.70
total	100

Figure 4. Mineral composition of pyrite framboids in samples from the Ursula Creek and Chibi sections. (A) SEM image and EDS spectrum at the red cross of a pyrite framboid from the lower Fantasque Formation, Ursula Creek; (B) SEM image and EDS spectrum at the red cross of a pyrite framboid from the lower Grayling Formation, Ursula Creek; and (C) SEM image and EDS spectrum at the red cross of a pyrite framboid from the lower Talung Formation, Chibi.

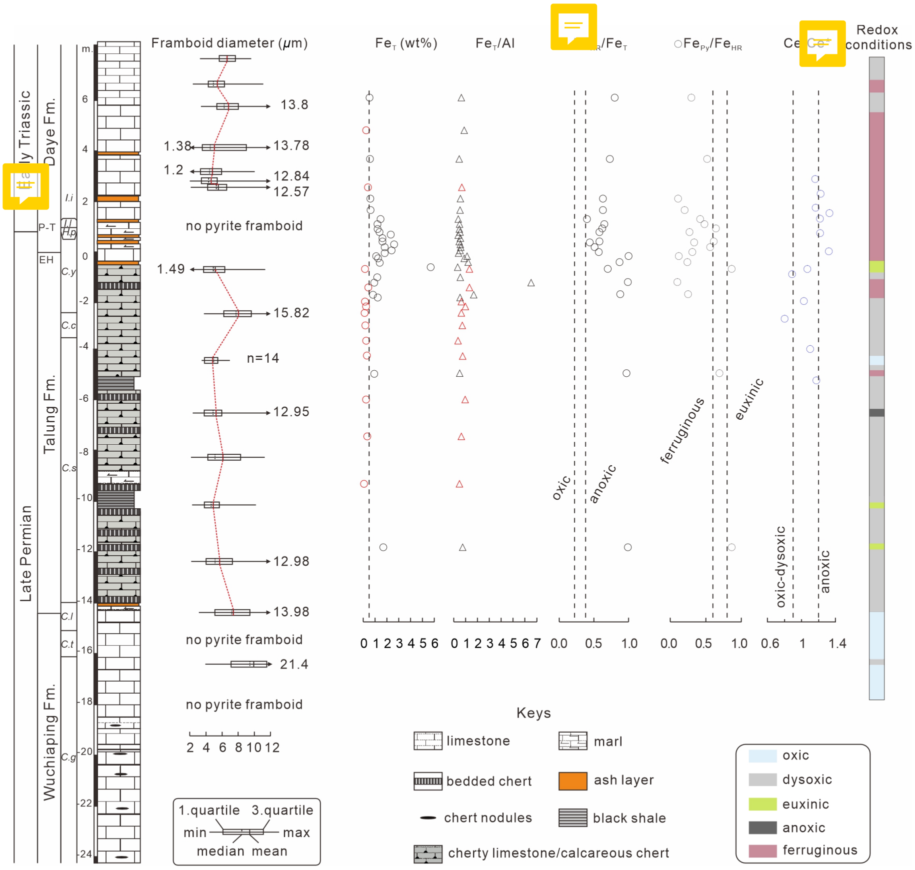

Figure 5. Stratigraphic log of the Chibi section with total iron (Fe_T), Fe_T/Al, iron proxies [Fe_{HR}/Fe_T, Fe_{Py}/Fe_{HR}, $(Fe_{Py}+Fe_{ox})/Fe_{HR}$, Fe_{ox}/Fe_{HR}], Ce-anomalies, and pyrite framboid "box-and-whisker" plots. Data of Ce-anomalies and framboids from Müller et al. (2023) and Yang et al. (2022) respectively.

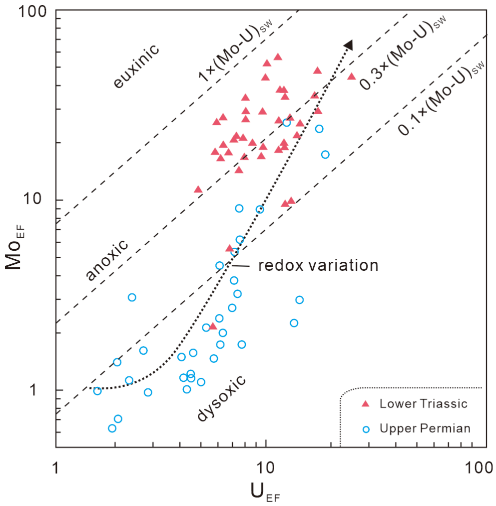

Figure 6. Covariation of Mo and U across the P-T transition at the Ursula Creek section. The "redox variation" pathway represents progressive redox shifts from dysoxic to euxinic conditions (modified from Algeo and Tribovillard, 2009).

https://doi.org/10.5194/egusphere-2026-863
Preprint. Discussion started: 26 February 2026

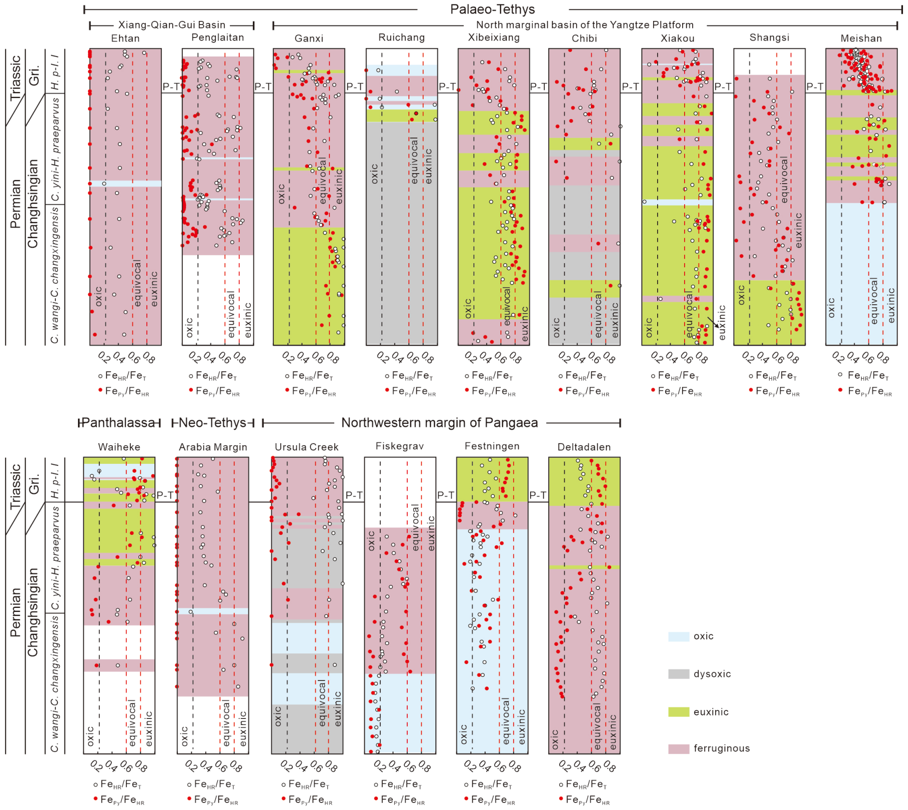

Figure 7. Palaeo-redox reconstruction via iron proxies across various sections situated in different palaeogeographic settings. Data sources: Waiheke, Takahashi et al. (2021); Arabia Margin, Clarkson et al. (2016); Ehtan and Ruichang, Yang et al. (2024); Penglaitan, Xiang et al. (2022); Ganxi, Lei et al. (2017); Xibeixiang, Ge et al. (2022); Xiakou, Shen et al. (2016); Shangsi, Xiang et al. (2016); Meishan, Xiang et al. (2020); Fiskegrav, Mettam et al. (2017); Festningen and Deltadalen, Schobben et al. (2020). Gri. - Griesbachian; *H. p* - *H. parvus*; *I. i* - *I. isarcica*.